

# Confined Crystallization of PEO in Nanolayered Films Impacting Structure and Oxygen Permeability

Haopeng Wang, Jong K. Keum, Anne Hiltner,\* and Eric Baer

Department of Macromolecular Science and Engineering, Case Western Reserve University, Cleveland, Ohio 44106-7202

Received June 26, 2009; Revised Manuscript Received August 3, 2009

**ABSTRACT:** Layer-multiplying coextrusion or “forced assembly” of thousands of alternating polystyrene (PS) and poly(ethylene oxide) (PEO) nanolayers was used to study crystallization in a confined, two-dimensional space. Atomic force microscopy and small-angle X-ray scattering revealed that as the thickness of the confined PEO layer decreased from the microscale to the nanoscale, the morphology of the PEO changed from three-dimensional spherulites to two-dimensional discoids and to “in-plane” lamellar stacks. Finally, when the confinement occurred on the 25 nm size scale of the usual lamellar thickness, the PEO layers crystallized as single lamellae with large aspect ratio that resembled large single crystals. This crystallization habit imparted more than 2 orders of magnitude reduction in oxygen permeability of the PEO layers. The oxygen permeability directly correlated with the orientation of the lamellar crystals. The dramatic decrease in oxygen permeability arose from a reduction in diffusivity due to increased tortuosity of the diffusion pathway through the oriented lamellae. However, the confined crystalline morphology did not affect the diffusion jump length of oxygen molecules, as reflected by the constant activation energy regardless of the layer thickness. At 85% relative humidity, the moisture sorption of PEO layers was consistently about 8%, independent of the layer thickness. Nevertheless, the lamellar orientation was not affected, and the dramatic decrease in PEO permeability was preserved.

## Introduction

It is well-known that crystallization reduces the gas permeability of polymer films.<sup>1</sup> The efficiency of chain packing in the crystalline phase reduces the free volume available for gas transport to such an extent that the crystalline phase may be regarded as impermeable relative to the amorphous phase and gas transport is seen as occurring through the amorphous regions only. The processing conditions can be readily varied to control the amount of crystallinity and chain orientation and thereby to tune the transport properties of the final product.<sup>2</sup> With the growing usage of polymers as thin and ultrathin films, unique crystalline morphologies have been found as a result of constrained two-dimensional crystallization.<sup>3,4</sup> These morphologies may impart gas transport characteristics that are not achievable in thicker films.

When a polymer crystallizes in a confined ultrathin layer, usually a few tens of nanometers, the isotropic spherulitic organization of lamellar crystals is prevented and instead, confinement can produce unique lamellar crystal orientations. In some cases, the preferred alignment of the chains is parallel to the layer plane and the crystals are found predominantly as “on-edge” lamellae. Reported examples include isotactic polypropylene (iPP),<sup>5</sup> polyethylene (PE),<sup>6</sup> polyamide-6,<sup>7</sup> poly(ethylene naphthalate) (PEN),<sup>8</sup> and poly(ethylene terephthalate) (PET).<sup>9</sup> However, at the other extreme, “in-plane” lamellae with chain orientation perpendicular to the layers are observed. Some examples are poly(ethylene oxide) (PEO),<sup>10,11</sup> isotactic polystyrene (iPS),<sup>12</sup> syndiotactic polypropylene (sPP),<sup>13</sup> poly(3-hydroxybutyric acid),<sup>14</sup> poly( $\epsilon$ -caprolactone) (PCL),<sup>15</sup> and poly(L-lactide) (PLA).<sup>16</sup>

The one-dimensional confinement of polymer crystallization is conventionally studied with a spin-coated thin layer on a substrate<sup>3</sup> or with block copolymers that contain at least one crystallizable block.<sup>10</sup> The conventional approaches have limitations. Spin-coating is limited by the solvent requirement, by the small amount of material that can be fabricated, and by the free surface, which can affect the properties of a spin-coated thin layer.<sup>17</sup> Self-assembled block copolymers require specific synthesis and shear alignment to construct the uniformly oriented phase structure.<sup>18</sup> In addition, covalent bonding between blocks adds another variable that can affect confined crystallization. An alternative approach is based on layer-multiplying coextrusion,<sup>19</sup> which forced assembly to create films with hundreds or thousands of alternating layers of two polymers with the thickness of nanometers.<sup>20</sup> The continuous confining layers provide long-range, almost defect-free confinement to study confined polymer crystallization. When iPP and PE were confined in coextruded nanolayers, on-edge lamellar orientation was observed.<sup>21</sup> However, when PEO nanolayers were confined by poly(ethylene-co-acrylic acid) (EAA) layers, single-layer in-plane lamellae were achieved.<sup>22</sup> They resembled the PEO single crystals that previously formed only in dilute solution. The degree of in-plane lamellar orientation in coextruded PEO nanolayers was much higher than in PEO diblock copolymers.<sup>10</sup>

With layer multiplying coextrusion, the confined layer thickness can be easily varied by several orders of magnitude, from the microscale to the nanoscale, without changing the molecular weight of the components, in contrast to block copolymers in which the confinement spacing relies on the molecular weight of the blocks.<sup>23</sup> Although the amount of material in a single layer is very small, the properties of the confined layer are multiplied many-fold by the number of identical layers in the film. This enables the use of conventional methods to probe size-scale-

\*Corresponding author: E-mail: ahiltner@case.edu.

**Table 1.** Film Composition, Number of Layers, Film Thickness, Nominal Layer Thickness, and the Thermal Characteristics of PS/PEO Films

sample	PS/PEO		nominal layer thickness (nm)				density (g/cm <sup>3</sup> )	$T_{m,PEO}$ (°C)	$\Delta H_{m,PEO}$ (J/g)	$X_{c,PEO}$ (wt %)	$P(O_2)$ (barrier)	aspect ratio $\alpha$
	(v/v)	(w/w)	film thickness (μm)	PS	PEO							
PS control	100/0	100/0	127				1.048 ± 0.002				2.08 ± 0.01	
PEO control	0/100	0/100	127				1.217 ± 0.002	65	150	76	0.38 ± 0.01	
9-layer	50/50	49/51	279	35000	35000		65	150	76	0.63 ± 0.01		
	50/50	49/51	142	18000	18000	1.121 ± 0.004	65	141	72	0.50 ± 0.01		
	70/30	72/28	284	50000	21000		66	147	75	0.88 ± 0.05		
	70/30	72/28	135	23500	10100	1.081 ± 0.003	65	144	73	0.66 ± 0.01		
33-layer	50/50	49/51	130	4000	4000	1.117 ± 0.002	65	148	75	0.283 ± 0.003		
	70/30	72/28	137	6000	2600	1.090 ± 0.005	65	151	77	0.350 ± 0.001		
257-layer	50/50	49/51	254	1000	1000		65	142	72	0.158 ± 0.010		
	50/50	49/51	127	500	500	1.123 ± 0.003	65	144	73	0.098 ± 0.001		
	50/50	49/51	51	200	200	1.130 ± 0.005	64	143	73	0.047 ± 0.004		
	70/30	72/28	127	700	300	1.090 ± 0.005	64	140	71	0.096 ± 0.001		
	70/30	72/28	51	280	120	1.094 ± 0.007	64	143	73	0.046 ± 0.001	70	
1025-Layer	50/50	49/51	130	114	114	1.118 ± 0.003	64	142	72	0.0235 ± 0.0002	48	
	50/50	49/51	48	45	45	1.119 ± 0.007	64	138	70	0.0070 ± 0.0003	90	
	70/30	72/28	128	175	75	1.096 ± 0.005	63	148	75	0.0178 ± 0.0013	107	
	70/30	72/28	58	69	30	1.094 ± 0.004	64	145	73	0.0104 ± 0.0014	144	
	80/20	81/19	132	183	46	1.078 ± 0.004	63	137	70	0.0126 ± 0.0006	210	
	80/20	81/19	53	71	21	1.082 ± 0.009	63	140	71	0.0221 ± 0.0022	153	
	90/10	91.4/8.6	125	215	25	1.064 ± 0.003	63	133	68	0.0436 ± 0.0005	265	

dependent properties. As an example, the large, in-plane PEO lamellae unexpectedly reduced the gas permeability of PEO nanolayers by almost 2 orders of magnitude.<sup>22</sup>

Further exploration of the exciting results obtained with PEO nanolayers was hampered by the use of a semicrystalline polymer as the confining layers. In the present study, EAA was replaced with PS. This had several advantages. More precise X-ray analysis was possible without the interference from a second set of crystalline reflections. The higher modulus of glassy PS layer provided stronger confinement for the crystallization of the PEO layers. These advantages were exploited in the present study to probe the structural origins of the exceptionally low gas permeability.

## Materials and Methods

Poly(ethylene oxide) (PEO) with a molecular weight of 200 kg/mol (PolyOx WSR N-80) and polystyrene (PS) (STYRON 666D, MFI = 8.0, 200 °C/5.0 kg, ASTM D1238) were obtained from The Dow Chemical Company. Both PS and PEO were dried under vacuum before processing.

Films with alternating PS and PEO layers with PS outer layers were fabricated using the layer multiplication process described previously.<sup>24</sup> The extruder, multiplier elements and die temperatures were set to 200 °C to ensure matching viscosities of the two polymer melts. Films with 9, 33, 257, and 1025 alternating PS and PEO layers were coextruded. The composition ratio was varied as (PS/PEO) (v/v) 50/50, 70/30, 80/20 and 90/10. For each composition and number of layers, several film thicknesses, about 250, 125, and 50 μm, were produced. The nominal layer thickness was calculated from the number of layers, the composition ratio and the film thickness (Table 1). To determine the actual weight fraction of the PEO, the layered films with nine layers were immersed into water to dissolve the PEO layers. The residual PS layers were weighed and the weight fraction of PEO layers was calculated (Table 1). Nonlayered PS and PEO control films were also extruded. The films were stored at ambient temperature in desiccators to prevent moisture absorption.

Films were embedded in epoxy and cured at room temperature. Cross sections were microtomed at -80 °C perpendicular to the extrusion direction with a cryo-ultramicrotome (MT6000-XL from RMC, Tucson, AZ). The cross sections were examined with an atomic force microscope (AFM) in order to visualize the layers

and the crystalline morphology. Phase and height images of the cross sections were recorded simultaneously at ambient temperature in air using the tapping mode of the Nanoscope IIIa Multi-Mode scanning probe (Digital Instruments, Santa Barbara, CA). Visual inspection by polarized optical microscopy (OM) was also performed in the transmission mode with an Olympus (Lake Success, NY) BH-2 microscope.

The film density was determined by hydrostatic weighing using a balance and a density determination kit (Mettler Toledo Model XS205). Iso-octane (99.8% pure, Sigma Aldrich) with a density of 0.692 g cm<sup>-3</sup> was used as the auxiliary liquid. Thermograms were obtained on a Perkin-Elmer (Boston, MA) Series 7 differential scanning calorimeter (DSC) at a heating/cooling rate 10 °C min<sup>-1</sup>. The crystallinity of the PEO control was 78 wt % calculated from the melting enthalpy using the heat of fusion ( $\Delta H^0$ ) of 197 J g<sup>-1</sup> for PEO crystals.<sup>25</sup> The crystallinity of the PEO layers was calculated based on the melting enthalpy of the PEO layers ( $\Delta H_{m,PEO}$ ) and the PEO weight content in the films (Table 1).

Small-angle X-ray scattering (SAXS) and wide-angle X-ray scattering (WAXS) patterns were obtained by aligning the incident X-ray beam parallel to the normal direction (ND), the extrusion direction (ED), or the transverse direction (TD) of the film. The SAXS measurements were carried out using a rotating anode X-ray generator (RU 300, 12 kW, Rigaku, Woodlands, TX) equipped with two laterally graded multilayer optics in a side-by-side arrangement, giving a highly focused parallel beam of monochromatic Cu K $\alpha$  radiation ( $\lambda = 0.154$  nm). The monochromatic X-ray beam, operated at 40 kV and 80 mA, was collimated using three pinholes. The diameter of the X-ray beam at the sample position was approximately 700 μm. For the collection of ED and TD SAXS patterns, because the thickness of the films (50–250 μm) was smaller than the collimated X-ray beam, the X-ray beam was aligned at an angle of ~3° relative to the ED and the TD to avoid total reflection. The critical angle for the total reflection is usually on the order of a few tenths of a degree. In order to collect ND SAXS patterns, the X-ray beam was aligned along the direction parallel to the ND. Two dimensional (2D) SAXS patterns were collected by using a 2D gas filled multiwire detector (Rigaku) with a spatial resolution of 1024 × 1024 pixels. The X-ray exposure time for ED, TD, and ND SAXS patterns was 9 h. The sample-to-detector distance was 1.5 m

and the scattering vector  $q$  was calibrated using a silver behenate (AgBe) standard, which has the (001) peak position at  $q = 1.076 \text{ nm}^{-1}$ . A photodiode beam stop placed in front of the area detector allowed monitoring of the intensity of the direct beam. On the basis of the intensity of the direct beam, all SAXS images were corrected for background scattering and sample absorption. The WAXS measurements were performed using the same rotating anode X-ray generator. The collimated beam size was 0.5 mm. The 2D patterns were collected with a Bruker AXS (Madison, WI) HI-STAR area detector. The sample-to-detector distance was 74 mm and the diffraction angle was calibrated using a CaF<sub>2</sub> standard.

Oxygen flux  $J(t)$  at 0% relative humidity, 1 atm pressure, and temperatures ranging from 23 to  $-10^\circ\text{C}$  ( $\pm 0.1^\circ\text{C}$ ) was measured with a MOCON (Minneapolis, MN) OxTran 2/20 fitted with a remote diffusion cell and a Thermo-Neslab thermal bath. The instrument was calibrated at  $23^\circ\text{C}$  with NIST-certified Mylar film of known oxygen transport characteristics. The specimens were carefully conditioned in the instrument, as described previously.<sup>26</sup> The permeability  $P$  was first calculated from the steady state flux  $J$  as

$$P = J \frac{l}{\Delta p} \quad (1)$$

where  $l$  is the film thickness and  $\Delta p$  is the difference of the oxygen partial pressure across the film (1 atm). For each film, the average  $P$  and error bar from two specimens were reported. To obtain the diffusivity  $D$  and to accurately determine the permeability  $P$ , the data were fit to the solution of Fick's second law with appropriate boundary conditions.<sup>26</sup>

$$J(t) = \frac{P\Delta p}{l} \left[ 1 + 2 \sum_{n=1}^{\infty} (-1)^n \exp\left(-\frac{D\pi^2 n^2 t}{l^2}\right) \right] \quad (2)$$

The error in determining the two fitting parameters,  $P/l$  and  $D/l^2$ , was estimated not to exceed 2%.<sup>26</sup> The average thickness  $l$  of each specimen was determined as  $l = M(A\rho)^{-1}$ , where  $M$  is the specimen mass,  $A$  is the specimen area and  $\rho$  is the density. The solubility  $S$  was obtained from the relationship  $P = DS$ . To obtain the nonsteady state  $J(t)$ , the characteristic response time of the Mocon oxygen sensor required that the time to reach equilibrium flux had to exceed 0.8 h.<sup>27</sup> For the relatively thin layered films, the nonsteady state  $J(t)$  could only be obtained reliably at subambient temperatures. For the PS and PEO controls, thicker 0.5 mm extruded films were used for nonsteady flux measurements all temperatures studied.

To study the effect of relative humidity (RH) on oxygen permeability, PS/PEO layered films were dried at  $23^\circ\text{C}$  for 48 h in vacuum and were exposed to a precisely controlled 85% RH at  $23^\circ\text{C}$ . The 85% RH was maintained with a saturated potassium chloride (KCl) aqueous solution in accordance with ASTM E 104-85. The specimens were weighed periodically until a constant weight was achieved. The moisture sorption was defined as the weight percentage of the absorbed water with respect to the original mass of the dry specimen. Results from three specimens were reported for each film. Oxygen permeability was also measured on the conditioned films at  $23^\circ\text{C}$  with the MOCON Oxtran2/20 with the RH adjusted to 85%.

## Results and Discussion

**Morphology of PEO Layers.** The use of a transparent, glassy polymer to confine the crystallizable PEO layers in the PS/PEO layered assemblies allowed the spherulitic structure of the PEO layers to be observed in the polarized optical microscope. A series of micrographs in Figure 1 revealed the characteristic Maltese cross pattern of spherulite-like structures in PEO layers as thin as 300 nm. The negative

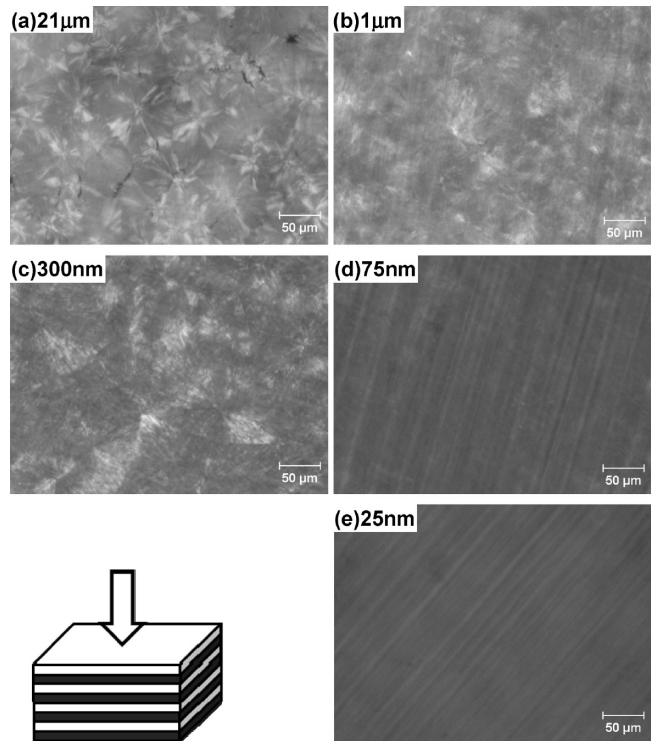


**Figure 1.** Polarized optical micrographs of PS/PEO layered films: (a) 21  $\mu\text{m}$ , (b) 1  $\mu\text{m}$ , (c) 300 nm, (d) 75 nm, and (e) 25 nm PEO layers.

birefringence indicated that the lamellae were oriented radially with the chain direction tangential as is typical for PEO spherulites.<sup>28</sup> Because the lateral (in-plane) diameter of the spherulites was larger than the PEO layer thickness, the spherulites in the 21  $\mu\text{m}$  PEO layers were somewhat truncated, rather than isotropic. In 1  $\mu\text{m}$  and 300 nm PEO layers, the average lateral dimension of the spherulite-like structures (80 and 100  $\mu\text{m}$ ) greatly exceeded the layer thickness. These structures were described as discoids. The Maltese cross pattern was absent from films with 75 and 25 nm thick PEO layers. Instead, only uniform, very weak birefringence suggested a different crystal habit in PEO nanolayers.

The AFM images of the film cross sections showed that in all cases, the layers were continuous and the average layer thickness corresponded closely to the nominal layer thickness. From the AFM images, the nominally 75 nm layers measured  $79 \pm 23 \text{ nm}$  and the nominally 25 nm layers measured  $26 \pm 7 \text{ nm}$ . The truncated spherulites in the film with 21  $\mu\text{m}$  thick PEO layers nucleated predominantly within the PEO layer, Figure 2a. The crystallization habit closely resembled that of PEO in the bulk with radial growth of 25 nm thick lamellae. The discoids in 1  $\mu\text{m}$  PEO layers nucleated primarily from the interface, Figure 2b. The lamellar growth in the layer thickness direction was highly constrained by the PS layers so that the long radial lamellae were preferentially oriented into the layer plane. In the 300 nm PEO layers the lamellae appeared to grow in stacks that were predominantly oriented in the plane of the layer, Figure 2c. Some out-of-plane twist of the lamellae was indicated by existence of discoids with the characteristic Maltese cross pattern (Figure 1c). The confined 75 nm thick PEO layers crystallized as stacks of three to five long lamellae, Figure 2d. Most of the lamellae were oriented in the plane of the layer. Because the chains of the in-plane lamellae were parallel to the film normal direction, they did not generate a Maltese cross pattern in the OM, Figure 1d. Chains in the tilted lamellae contributed to the very weak birefringence.

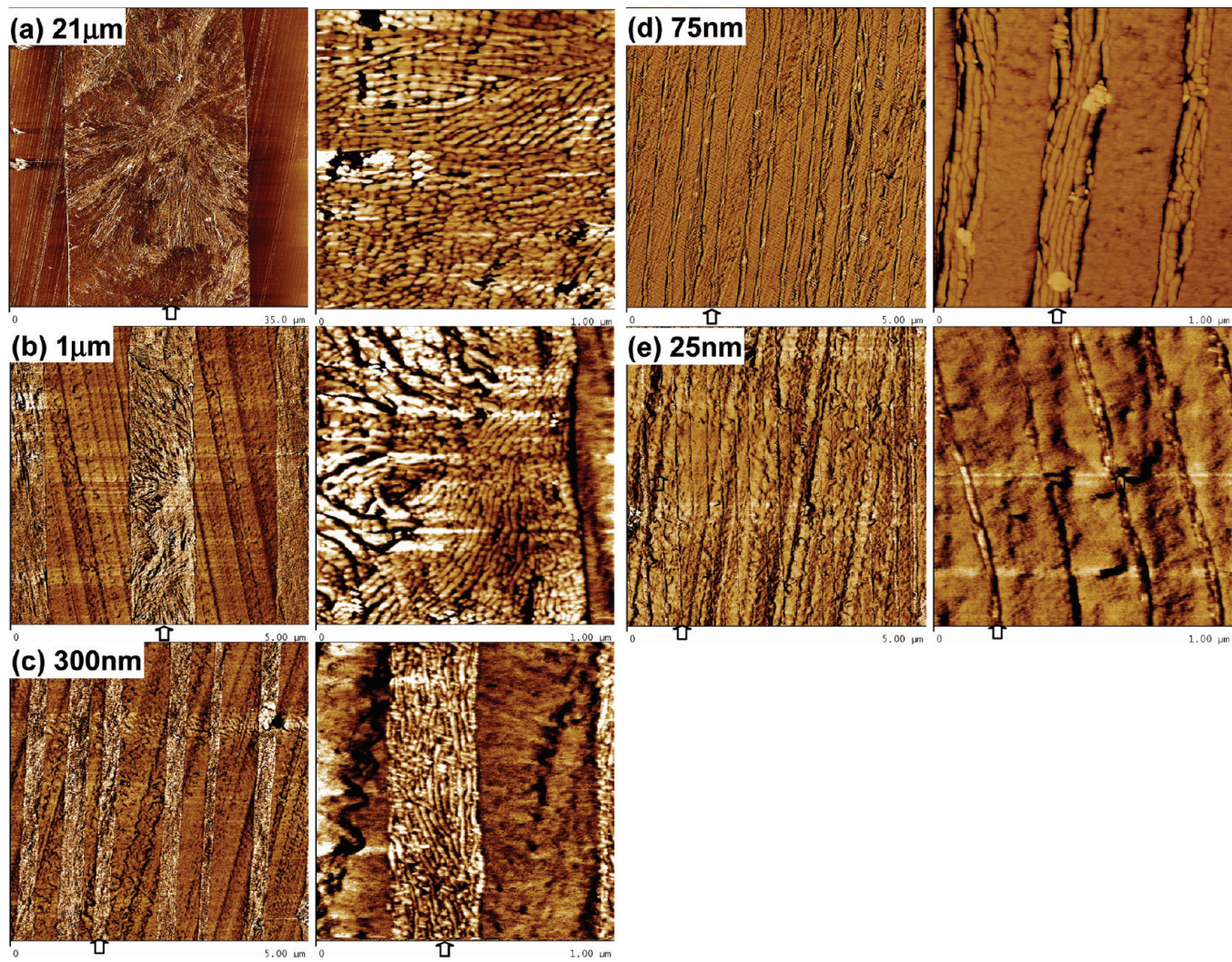


**Figure 2.** AFM phase images of partial cross sections of PS/PEO layered films: (a)  $21\text{ }\mu\text{m}$ , (b)  $1\text{ }\mu\text{m}$ , (c)  $300\text{ nm}$ , (d)  $75\text{ nm}$ , and (e)  $25\text{ nm}$  PEO layers. Two magnifications of each film are shown. The images in the left column are  $5\text{ }\mu\text{m} \times 5\text{ }\mu\text{m}$  except that the image in part a is  $35\text{ }\mu\text{m} \times 35\text{ }\mu\text{m}$ ; the images in the right column are all  $1\text{ }\mu\text{m} \times 1\text{ }\mu\text{m}$ . The arrows indicate a PEO layer. The lines in the PS layers were knife marks from the cryo-micromotoming; otherwise the PS layers were featureless.

The 25 nm thick PEO layers crystallized as single very long, thin lamellae sandwiched between the thick PS layers, Figure 2e. It was thought that the coincidence between the layer thickness and the thickness of PEO lamellae facilitated crystallization of the layers as single lamellae. It was noteworthy that the lamellar thickness remained the same regardless of the layer thickness.

Upon cooling, the crystallization temperature  $T_{c,\text{PEO}}$  of  $40\text{ }^\circ\text{C}$  was only  $5\text{ }^\circ\text{C}$  lower than that of the PEO control. Most studies put the temperature for homogeneous nucleation of PEO between  $-10$  and  $0\text{ }^\circ\text{C}$ .<sup>29</sup> A crystallization temperature close to that of the bulk meant that the in-plane PEO lamellae nucleated on heterogeneous nuclei, such as catalyst residue, high-molecular-weight gel particles or dust particles.<sup>30</sup> Because the spherulites in the thicker layers and the single crystals in the nanolayers were very large, the concentration of these nuclei must have been very low. The distribution of the nuclei was random in the bulk, however with decreasing layer thickness, the probability of their locating at the layer interface increased. As a result, spherulites or lamellar stacks were seen to nucleate at the layer interface. These nuclei might have been oriented during extrusion, which would have facilitated the formation of in-plane PEO crystals.

**Lamellar Orientation in PEO Layers by SAXS.** The 2D SAXS patterns of all the films showed intense meridional streaks in the ED patterns that contained the overlapped scattering from the PEO lamellae, the PS/PEO interfaces, and the film surface, Figure 3. Although the scattering from the film surface and the interfaces tended to mask the relatively weak scattering from the PEO lamellae, certain features in the ED patterns were discerned. The PEO control revealed isotropic ED and ND patterns. However the ED pattern of the layered films appeared quite different. The  $21$  and  $1\text{ }\mu\text{m}$  PEO layers exhibited oriented two-arc scattering at the meridian in the ED patterns. As the PEO layer thickness decreased to  $300$  and  $75\text{ nm}$ , a two-spot scattering feature emerged at the meridian in the ED patterns. The strong meridional intensity in the ED patterns indicated that the normal of the lamellar fold surface was predominantly oriented toward the ND of the multilayered films. The appearance of spots rather than arcs indicated that the degree of lamellar orientation was very high. The ND patterns remained isotropic regardless of the PEO layer thickness.

For clarification, the meridional scattering profiles were extracted from the ED and ND patterns, Figure 4. Comparison of the scattering profiles indicated that the first-order peak position  $s^*$  of the PEO lamellar stacks remained nearly

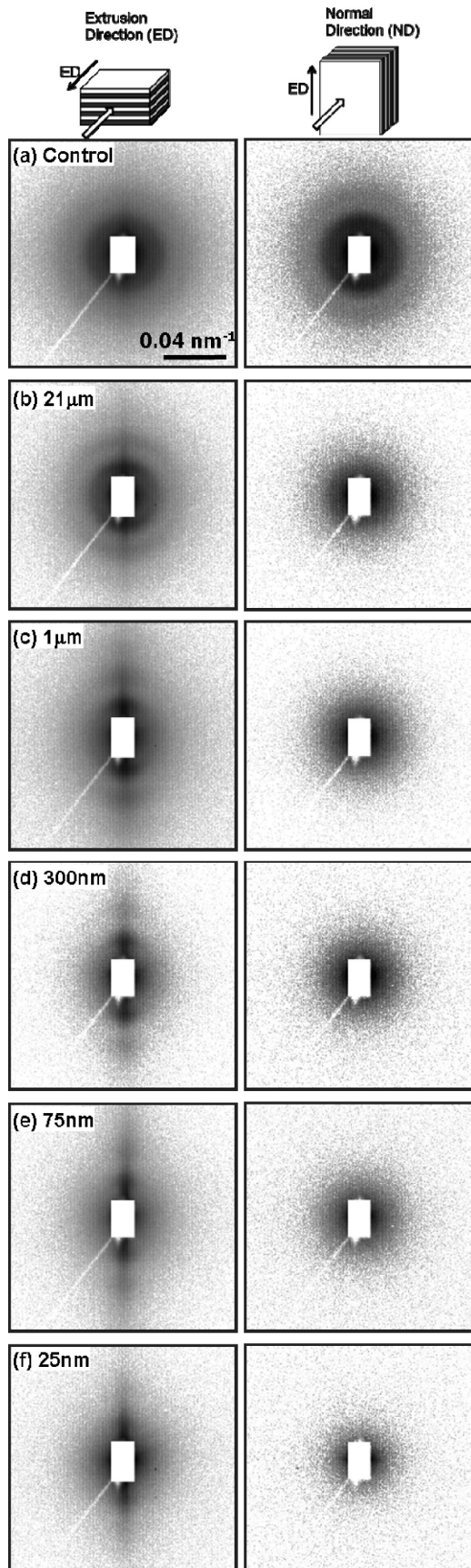


**Figure 3.** 2D SAXS patterns of: (a) PEO control; and PS/PEO layered films with the following PEO layer thickness: (b) 21  $\mu\text{m}$ ; (c) 1  $\mu\text{m}$ ; (d), 300 nm; (e), 75 nm; (f) 25 nm. The X-ray beam was aligned along the extrusion direction (ED, left column) and the normal direction (ND, right column). The scale bar in part a was drawn based on the scattering vector  $s$  scale.

the same. The corresponding long period  $L = 1/s^*$  was  $23 \pm 1$  nm. Here  $s$  is the scattering vector and its amplitude is related to the scattering angle  $2\theta$  and the X-ray beam wavelength  $\lambda$  as  $s = 2(\sin \theta)/\lambda$ . Both the magnitude and the consistency of the long period agreed with the AFM results. The peak in the ED patterns of the thicker PEO layers was much stronger in intensity and sharper than those in the ND patterns, where the pattern was barely discernible, indicating that the normal direction of the PEO lamellae was predominantly oriented along the ND. When the PEO layer thickness was reduced to 25 nm, corresponding to the lamellar thickness, the first order correlation peak in the ED pattern was highly suppressed compared to those in the thicker layers. This implied that the confinement at 25 nm, comparable to the long period of the lamellae, prevented the stacking of lamellae. If the lamellae were uncorrelated in 25 nm PEO layers, they would not exhibit a first-order peak maximum in the SAXS pattern and would only show an asymptotic decay in the scattering with  $s$ . The observed weak correlation peak from the 25 nm PEO layers was associated with the thickness distribution of the PEO layers which occasionally enabled the formation of two lamellae in a single PEO layer. In the ND pattern, on the other hand, no first-order peak maximum was detected implying a single population of in-plane lamellae that had grown in the direction parallel to the PEO layers.

**Crystal Orientation in PEO Layers by WAXS.** The ED and ND WAXS patterns from the PEO control exhibited isotropic diffraction rings. The first ring (scattering angle  $2\theta = 19.2^\circ$ ) consisted of the reflections from PEO (120) planes and the second ring ( $2\theta = 23.3^\circ$ ) contained the overlapping reflections from the (032), ( $\bar{1}32$ ), (112), ( $\bar{2}12$ ), ( $\bar{1}24$ ), (204) and (004) planes, which have similar  $d$ -spacing of  $\sim 0.39$  nm. These reflections were typical of the monoclinic crystal form of PEO.<sup>31</sup> For the PS/PEO layered films, the same reflections were observed for the PEO layers, in addition to the amorphous halo from the PS layers at  $2\theta = 18.7^\circ$ . Because the WAXS patterns measured in the TD were indistinguishable from those in the ED, only ED patterns are presented here. The ED pattern of layered films with 21  $\mu\text{m}$  thick PEO layers showed a slight orientation with two broad PEO (120) diffraction arcs centered at the equator, Figure 5a. This orientation was attributed to the truncation of the PEO spherulites in the thickness direction.

The ED pattern from the film with 1  $\mu\text{m}$  PEO layers revealed considerable orientation, Figure 5b. The PEO (120) reflections appeared as short equatorial arcs and the PEO (032) reflections as arcs at approximately  $67^\circ$  with respect to the meridian. In the third reflection ring, very weak ( $\bar{2}24$ ) and (024) reflections appeared at  $45^\circ$  with respect to the meridian. Decreasing the PEO layer thickness to 300 and 75 nm sharpened the diffraction arcs in the ED pattern, Figure 5c,d, until they became spots when the PEO layer thickness was 25 nm, Figure 5e. The ED pattern of the films with 25 nm PEO layers resembled the PEO fiber pattern,<sup>32</sup> and indicated that the  $c$ -axis of the PEO crystals was well oriented along the ND, i.e. vertical to the layer plane.

The in-plane lamellar orientation in coextruded PS/PEO nanolayer films was much higher than that previously observed in PS-PEO block copolymers. The sharp diffraction spots in the ED WAXS patterns of the 25 nm PEO layers contrasted with the broad diffraction arcs reported for the PEO blocks in the block copolymers.<sup>10</sup> The higher orientation could be attributed to the rigid, “defect-free” confinement provided by the continuous PS layers. The absence of covalent bonds between the PS and PEO layers resulted in a sharper interface. Constraints imposed by the covalent

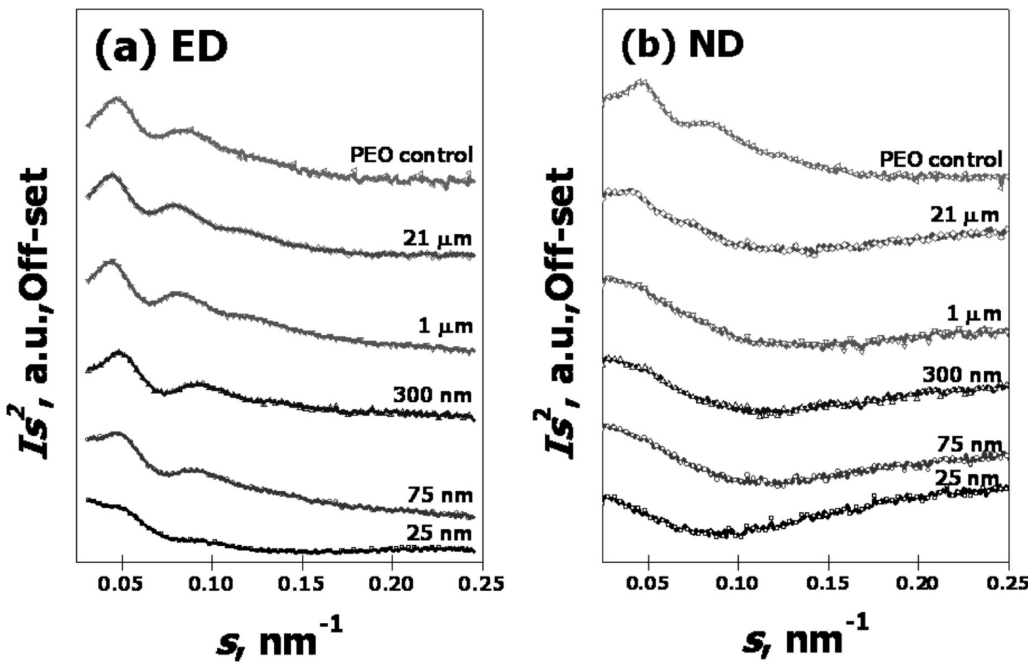


**Figure 4.** Meridional SAXS profiles from top to bottom of the PEO control and PS/PEO layered films with PEO layer thicknesses of 21  $\mu\text{m}$ , 1  $\mu\text{m}$ , 300 nm, 75 nm, and 25 nm. The profiles were extracted at the meridian of the corresponding ED (a) and ND (b) SAXS patterns in Figure 3.

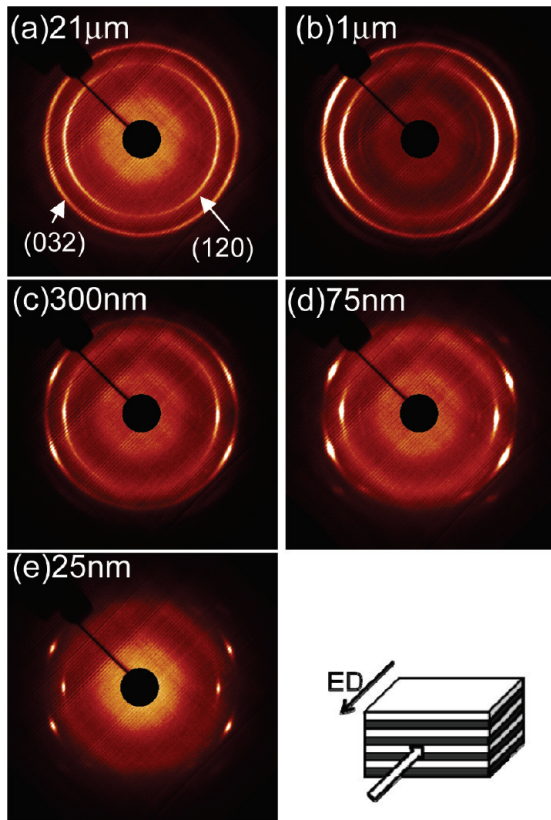


**Figure 5.** ED WAXS patterns of PS/PEO layered films with nominal PEO layer thickness as follows: (a) 21  $\mu\text{m}$ ; (b) 1  $\mu\text{m}$ ; (c) 300 nm; (d) 75 nm; (e) 25 nm. The X-ray beam was aligned along the extrusion direction (ED) of the layered films.

bonds could have caused crowding at the interface and poor crystal orientation in block copolymers. Furthermore, high molecular weight PEO was used in the coextrusion process, and fewer chain end defects would have enhanced the lateral growth of ordered lamellae.

Ideally, the orientation function can be quantitatively calculated from the azimuthal intensity distributions in the ED SAXS patterns. In this study, due to the intense grazing incidence scattering in the meridional direction of the ED SAXS patterns (Figure 3), an accurate measurement of the orientation function of the lamellar plane from SAXS could not be conducted. However, because the PEO (120) plane was perpendicular to the lamellar fold surface,<sup>33</sup> the orientation function of the PEO (120) plane denoted the lamellar orientation. The Hermans orientation function<sup>34</sup> was calculated from the azimuthal intensity distributions of the (120) reflection measured on the WAXS ED pattern. After the background and the amorphous contribution were subtracted from the intensity distribution, the Hermans orientation function  $f_{120}$  was calculated as

$$\langle \cos^2 \phi_{120} \rangle = \frac{\int_0^\pi I_{120}(\phi) \cos^2 \phi \sin \phi d\phi}{\int_0^\pi I_{120}(\phi) \sin \phi d\phi} \quad (3)$$

$$f_{120} = \frac{3\langle \cos^2 \phi_{120} \rangle - 1}{2} \quad (4)$$

where  $I_{120}(\phi)$  is the corrected scattered intensity of the PEO (120) reflection at the azimuthal angle  $\phi$ . The normal of the film plane is set to be  $\phi = 0^\circ$  and the film plane corresponds to  $\phi = 90^\circ$ ; then  $\phi_{120}$  is the angle between the normal of the film plane and the normal of the (120) plane. From the definition of the Hermans orientation function,  $f_{120} = -0.5$  indicates that the normal of the (120) plane is perfectly perpendicular to the layer normal, whereas  $f_{120} = 0$  corresponds to the perfectly random orientation. The azimuthal intensity distribution for the (120) reflection of the 25 nm thick PEO layer ED pattern is shown in Figure 6a. It was evident that the (120) intensity was concentrated at  $\phi = 90^\circ$ . The  $f_{120}$  for the 25 nm thick PEO layers was calculated to be  $-0.49$ . Thus, the (120) planes were highly oriented normal to the layer plane and the PEO lamellae were predominantly parallel to the layers at this layer thickness.

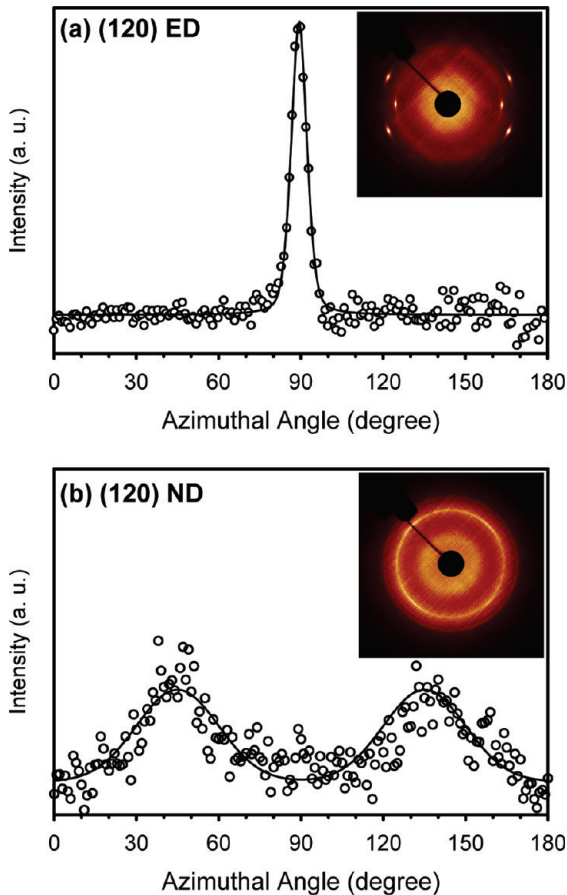


**Figure 6.** Azimuthal intensity profile for the PEO (120) reflection from the ED (a) and the ND (b) WAXS patterns of the 25 nm PEO layer. In part a, the layer normal was set at  $\phi = 0^\circ$  and the layer plane corresponded to  $\phi = 90^\circ$ . In part b, the extrusion direction was set at  $\phi = 0^\circ$  and the transverse direction of the film plane corresponded to  $\phi = 90^\circ$ . The solid lines are drawn as guides to the experimental data (open symbols).

The calculated values of  $f_{120}$  are plotted as a function of PEO layer thickness in Figure 7. Because there was a slight lamellar orientation in the thickest PEO layer ( $30 \mu\text{m}$ ), the isotropic (120) orientation ( $f_{120} = 0$ ) was not obtained. The decrease in  $f_{120}$  with decreasing PEO layer thickness was almost linear when the PEO layer thickness was plotted on a logarithmic scale. For very thin layers,  $f_{120}$  was less affected by layer thickness and gradually approached the limiting value of  $-0.5$  for 25 nm layers with single-layer, in-plane PEO lamellae. The orientation function was also calculated for the EAA/PEO layered films,<sup>22</sup> and the data are included in the figure for comparison. In the EAA/PEO layered films, the isotropic orientation ( $f_{120} = 0$ ) was observed in the thicker PEO layers, and  $f_{120}$  started to decrease only when the layer thickness was about  $1 \mu\text{m}$ . The EAA/PEO films had consistently lower degree of orientation (higher  $f_{120}$ ) than the PS/PEO films.

A couple of factors might have explained the substantial effect of the confining polymer. One was the stiffness of the confining layer. The PS layer vitrified at a higher temperature ( $T_{g,\text{PS}} = 98^\circ\text{C}$ ) than the EAA layer ( $T_{c,\text{EAA}} = 82^\circ\text{C}$ ), although both were higher than the crystallization temperature of PEO ( $T_{c,\text{PEO}} = 45^\circ\text{C}$ ). The entire PS layer vitrified at  $T_{g,\text{PS}}$  whereas only 34 wt % of the EAA layer solidified by crystallization at  $T_{c,\text{EAA}}$ . In addition, a slower cooling condition was used when the PS/PEO films were coextruded. The collecting roll temperature was  $95^\circ\text{C}$  for processing

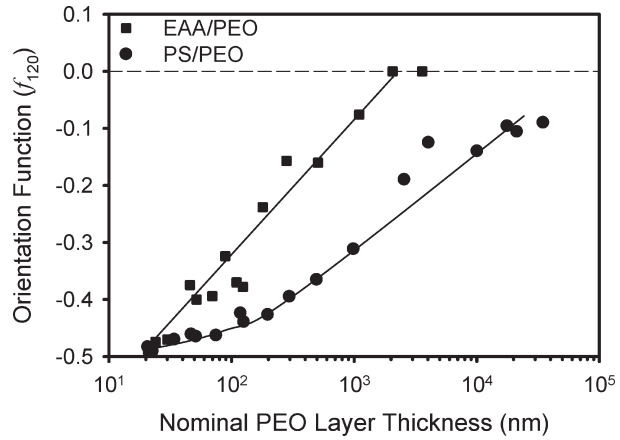


**Figure 7.** Effect of layer thickness on the orientation function  $f_{120}$  of the PEO (120) plane from the ED WAXS pattern of PS/PEO (●) and EAA/PEO (■) layered films. The solid lines are drawn as guides.

PS/PEO films, but  $25^\circ\text{C}$  for EAA/PEO films. The faster cooling rate and faster crystallization rate would have produced more nuclei, thereby resulting in lamellae with reduced lateral size and poorer orientation.

In addition to the in-plane lamellar orientation in the PS/PEO film with 25 nm PEO layers, the ND WAXS pattern of this film showed four broad (120) diffraction arcs centered at  $\pm 45^\circ$  with respect to the ED, Figure 6b. This 4-arc pattern indicated some preferred orientation of the PEO (120) planes at an angle of  $45^\circ$  with respect to the extrusion direction. The 4-arc pattern was analogous to the 4-point electron diffraction pattern of PEO single crystals.<sup>33</sup> This orientation was attributed to the effect of nanoscale confinement on the melt flow. Possibly the melt multiplication and the subsequent spreading into a thin film resulted in a preferred chain orientation  $45^\circ$  with respect to the ED.<sup>35</sup> As a result, orientation of the (120) growth plane<sup>33</sup> at  $45^\circ$  would have been kinetically favored. Alternatively, the flow might have produced a preferred orientation of the heterogeneous nuclei. With increasing PEO layer thickness the 4-arc ND pattern was lost and the ND WAXS patterns showed isotropic diffraction rings.

**Gas Permeability of PS/PEO Layered Films.** Figure 8a shows the oxygen permeability ( $P$ ) of a series of PS/PEO films with the same 50/50 composition but with different layer thicknesses. The layer thickness was varied by changing the number of coextruded layers and the overall film thickness (Table 1). The oxygen permeability decreased steadily as the PS and PEO layers became thinner. The gas permeability of a layered assembly can be calculated from the series model as

$$P_{//} = \left( \frac{\phi_{\text{PEO}}}{P_{\text{PEO}}} + \frac{1 - \phi_{\text{PEO}}}{P_{\text{PS}}} \right)^{-1} \quad (5)$$

where  $\phi_{\text{PEO}}$  is the volume fraction of PEO, and  $P_{\text{PEO}}$  and  $P_{\text{PS}}$  are the permeabilities of PEO and PS control films, respectively. Using the determined values of 0.38 barrer<sup>36</sup> and 2.08 barrer for  $P_{\text{PEO}}$  and  $P_{\text{PS}}$ , eq 5 gave the oxygen permeability of a PS/PEO 50/50 layered film as 0.64 barrer. It was found that only the 50/50 PS/PEO film with the thickest layers ( $35 \mu\text{m}$ ) conformed to this predicted value. In the PS/PEO 50/50 film with 47 nm layers,  $P$  was  $0.0070 \pm 0.0003$  barrer, corresponding to almost a 100-fold decrease. This  $P$  value was also well below the reported oxygen permeabilities, measured at  $23^\circ\text{C}$  and 0% RH, of some widely used oxygen barrier polymers, such as oriented poly(ethylene

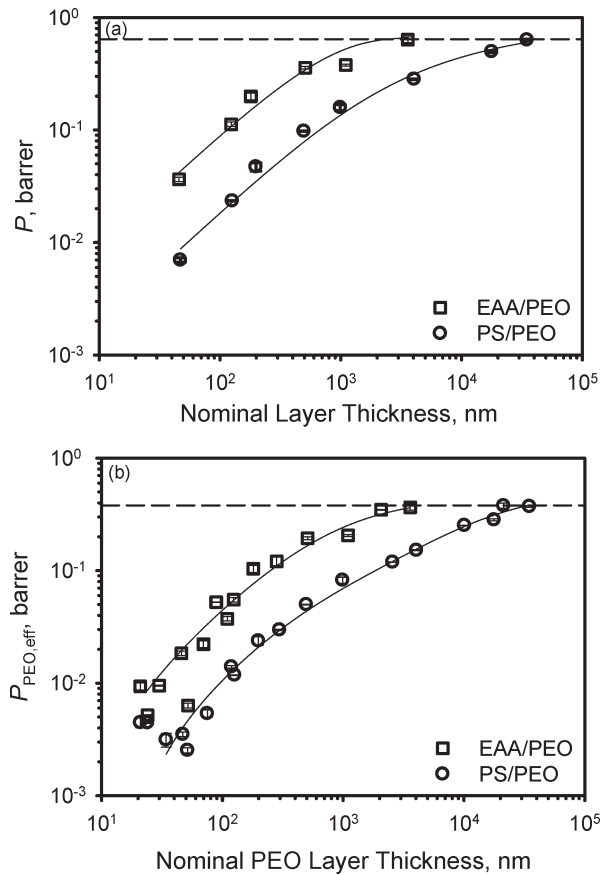


**Figure 8.** Effect of layer thickness on oxygen permeability at 23 °C and 0% RH. (a) Oxygen permeability of PS/PEO 50/50 films. The dashed line indicates  $P_l$  calculated from eq 5. (b) The effective PEO layer permeability  $P_{\text{PEO,eff}}$  from films of varying composition calculated from eq 6. The data of EAA/PEO layered films are taken from the literature.<sup>22</sup> The solid lines are drawn as guides. The dashed line indicates  $P_{\text{PEO}}$ .

terephthalate) (0.030 barrer),<sup>37</sup> Nylon6 (0.019 barrer),<sup>38</sup> or Nylon6,6 (0.010 barrer),<sup>39</sup> and the aromatic polyamides based on hexamethylenediamine (around 0.02 barrer).<sup>40</sup> For comparison, Figure 8a includes data for EAA/PEO films.<sup>22</sup> The  $P$  of the EAA/PEO films was generally about 4 to 5 times higher than that of the PS/PEO films at the same layer thickness. The permeability of the EAA control film ( $P_{\text{EAA}}$ ) was measured to be 2.30 barrer, very close to that of the PS control (2.08 barrer). Therefore the higher  $P$  of EAA/PEO layered films could not be attributed to the small difference between  $P_{\text{EAA}}$  and  $P_{\text{PS}}$ . Furthermore, noting that PEO is substantially less permeable to oxygen than either PS or EAA, eq 5 predicts that  $P$  will be quite sensitive to  $P_{\text{PEO}}$  even if  $\phi_{\text{PEO}}$  is relatively small. Therefore, the dramatic decrease in  $P$  of the layered films was attributed to a change in  $P$  of the PEO layers.

The effective PEO layer permeability,  $P_{\text{PEO,eff}}$ , in the layered films was calculated according to

$$P_{\text{PEO,eff}} = \phi_{\text{PEO}} \left( \frac{1}{P} - \frac{1-\phi_{\text{PEO}}}{P_{\text{PS}}} \right)^{-1} \quad (6)$$

Although the measured values of  $P$  scattered, depending on the composition ratio, the data of PS/PEO layered films collapsed to a single curve when plotted as a function of the PEO layer thickness, Figure 8b. Only  $P_{\text{PEO,eff}}$  of the thick PEO layers was close to  $P_{\text{PEO}}$ , as indicated by the dashed line in the figure. Deviation below the line was seen with 10 μm

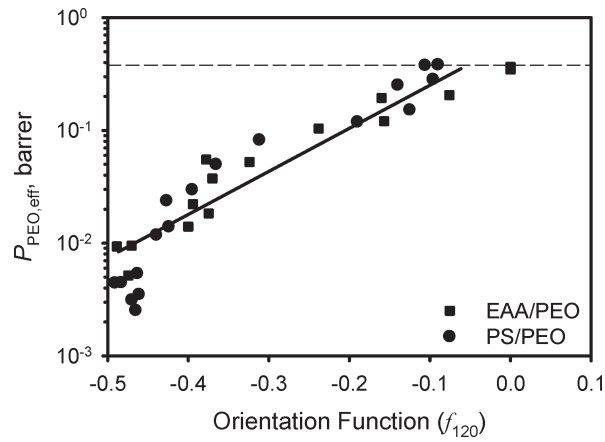


**Figure 9.** Correlation of the effective oxygen permeability of the PEO layer  $P_{\text{PEO,eff}}$  with the orientation function  $f_{120}$  of the PS/PEO (●) and EAA/PEO (■) layered films. The solid line is drawn as a guide. The dashed line indicates  $P_{\text{PEO}}$ .

thick PEO layers in PS/PEO films. The lowest  $P_{\text{PEO,eff}}$  achieved was 0.0025 barrer for 50 nm thick layers or about 1/150 of  $P_{\text{PEO}}$ . A slightly higher  $P_{\text{PEO,eff}}$  for films with the thinnest PEO layers was attributed to some layer breakup. The EAA/PEO films exhibited a parallel dependence of  $P_{\text{PEO,eff}}$  on layer thickness, however deviation from  $P_{\text{PEO}}$  started at a layer thickness of 1 μm and  $P_{\text{PEO,eff}}$  of the EAA/PEO films was consistently 4 to 5 times higher than in the PS/PEO films.

**Correlation of Gas Permeability with Lamellar Morphology.** The crystallinity of PEO in the layered films,  $X_{c,\text{PEO}}$ , as determined from the first heating DSC thermogram, was not affected by decreasing layer thickness, Table 1. The melting temperature of the PEO remained almost constant at 65 °C, the same as the PEO control. Therefore, the very low permeability of the PEO layer was attributed to the unusual crystalline morphology that resulted from confined crystallization. To find the general correlation between oxygen permeability and the degree of in-plane lamellar orientation, the effective PEO layer permeability  $P_{\text{PEO,eff}}$  was plotted as a function of the Hermans orientation function  $f_{120}$  in Figure 9. The data for PS/PEO and EAA/PEO films generally fell on a single linear correlation ln  $P$ . However, for very thin PEO layers,  $P_{\text{PEO,eff}}$  of the PS/PEO films was substantially lower than that of the EAA/PEO films. Because the orientation was almost at the limit of -0.50 for perfectly in-plane lamellae, the lower  $P_{\text{PEO,eff}}$  of the PS/PEO films suggested that the lateral dimension of the PEO lamellae in the PS/PEO films might be larger than in EAA/PEO films.

The lateral dimension of PEO lamellae can be estimated from the Cussler model,<sup>41</sup> which was often used to describe the gas permeability of a polymer composite with a dispersion of impermeable platelets. If the platelets are oriented at a fixed angle to the flux, the permeability is expressed as

$$P = P_m \left[ 1 + \frac{\alpha^2 \phi^2}{4(1-\phi)} \cos^2 \theta \right]^{-1} \quad (7)$$

where  $P_m$  is the permeability of the matrix,  $\phi$  is the volume fraction of impermeable platelets,  $\alpha$  is the aspect ratio of the platelets defined as the length divided by the thickness, and  $\theta$  is the angle between the flux and the normal to the platelets. In the nanolayered films, the PEO lamellar crystalline core was considered impermeable and the lamellar fold surfaces constituted the permeable amorphous regions. Gas molecules were seen as permeating through the defect regions

at the interlamellar boundaries. When the PEO lamellae were well oriented perpendicular to the gas flux ( $\cos^2 \theta \approx 1$ ), the permeability of the nanolayered composite could be described by

$$P = P_{\text{PS}} \left[ 1 + \frac{\alpha^2 \phi^2}{4(1-\phi)} \right]^{-1} \quad (8)$$

where  $\phi$  is the volume fraction of impermeable crystalline core and  $\alpha$  is the aspect ratio of the lamellae defined as the lateral length  $L$  divided by the thickness  $W$  of the crystalline core. In this case,  $\phi$  was taken as the volume fraction of the PEO crystalline phase in the total PS/PEO films and could be estimated from

$$\phi = X_{c,\text{PEO}} \times w_{\text{PEO}} \times \frac{\rho}{\rho_c} \quad (9)$$

where  $X_{c,\text{PEO}}$  is the crystallinity of the PEO layer in weight percent,  $w_{\text{PEO}}$  is the weight fraction of PEO layer in the film,  $\rho$  is the film density and  $\rho_c$  is the PEO crystal density,  $1.234 \text{ g cm}^{-3}$ .<sup>42</sup> For the PS/PEO layered film with 25 nm thick PEO layers, the aspect ratio was estimated from eq 8 to be 265. From small-angle X-ray scattering, the lamellar thickness of was determined to be  $23 \pm 1 \text{ nm}$  and the thickness of the crystalline core was estimated from PEO crystallinity as 16 nm. Thus the lateral dimension of the PEO lamellae could be more than  $4 \mu\text{m}$ . In contrast, the lateral dimension estimated for PEO lamellae in EAA/PEO films was about  $2 \mu\text{m}$ .<sup>22</sup>

Gradually increasing the PEO layer thickness relaxed the restriction on three-dimensional growth, which allowed crystallization of lamellar stacks and permitted randomization of the lamellar orientation. In addition, the increased area density of nuclei in a layer reduced the lateral dimension of the lamellae. The structure was modeled as a dispersion of impermeable platelets dispersed in a matrix of permeable interlamellar amorphous regions, and eq 7 was used to estimate the aspect ratio of the PEO lamellae. Due to some randomization of the lamellar orientation,  $\cos^2 \theta$  deviated from 1. Because the PEO (120) plane was perpendicular to the lamellar fold surface,  $\cos^2 \theta$  could be obtained from the geometrical relationship

$$\langle \cos^2 \theta \rangle = 1 - 2\langle \cos^2 \phi_{120} \rangle \quad (10)$$

where  $\cos^2 \phi_{120}$  is taken from eq 3. As the PEO layer thickness increased, the aspect ratio from eq 7 and the lamellar lateral dimension rapidly decreased, Table 1.

**Temperature Dependence of  $P$ ,  $D$ , and  $S$ .** On the basis of the solution-diffusion process, the permeability coefficient  $P$  of a polymer film is the product of the diffusivity  $D$  and the solubility  $S$ ,  $P = DS$ . If the dramatic decrease in  $P$  in layered films was due to an increase in the diffusion path length, the effect should have been observed in  $D$ , not  $S$ . The composite  $D$  of PS/PEO layered films was determined by fitting the experimental flux curve to Fick's second law (eq 2) with appropriate boundary conditions. Typical experimental oxygen flux curves in Figure 10 compare PS/PEO 50/50 films of similar film thickness ( $\sim 125 \mu\text{m}$ ) but different nominal layer thicknesses at  $0^\circ\text{C}$  and 0% RH. The initial increase in the oxygen flux reflected nonsteady-state diffusion. This part of the curve was determined by the diffusivity. The steady-state flux was determined by the permeability. The layer thickness had a strong effect on both the nonsteady-state and steady-state regions. Reducing the PEO layer thickness broadened the nonsteady-state region (lower  $D$ ) and dramatically decreased the steady-state flux

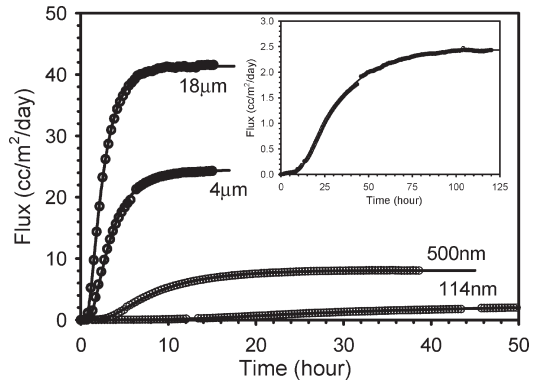


**Figure 10.** Experimental oxygen flux data at  $0^\circ\text{C}$  and 0% RH together with the fit to the solution of Fick's second law eq 2 (solid lines) for PS/PEO 50/50 films with thicknesses of about  $125 \mu\text{m}$ , but with various number of layers and nominal layer thicknesses. The nominal layer thickness is labeled next to each flux curve. The insert shows the complete flux curve for the films with 114 nm thick PEO layers.

(lower  $P$ ). However,  $S$  was not affected by layer thickness and maintained at a constant value of  $0.17 \pm 0.01 \text{ cm}^3(\text{STP}) \text{ cm}^{-3} \text{ atm}^{-1}$  at this temperature.

The temperature dependence of  $P$ ,  $D$ , and  $S$  for the same 4 films is plotted in Figure 11, together with PS and PEO controls, according to

$$P = P_0 \exp\left(-\frac{E_P}{RT}\right) \quad (11)$$

$$D = D_0 \exp\left(-\frac{E_D}{RT}\right) \quad (12)$$

$$S = S_0 \exp\left(-\frac{\Delta H_S}{RT}\right) \quad (13)$$

where  $E_P$  and  $E_D$  are the activation energies for permeation and diffusion,  $\Delta H_S$  is the heat of sorption,  $P_0$ ,  $D_0$  and  $S_0$  are preexponential factors,  $R$  is the gas constant and  $T$  is the temperature. Because the temperature range studied here,  $+15$  to  $-10^\circ\text{C}$ , is remote from any of the major transitions of the film components, such as  $T_{g,\text{PS}}$  ( $98^\circ\text{C}$ ),  $T_{m,\text{PEO}}$  ( $65^\circ\text{C}$ ) and  $T_{g,\text{PEO}}$  ( $-60^\circ\text{C}$ ),<sup>43</sup> the typical exponential dependence of  $P$ ,  $D$  and  $S$  on  $T^{-1}$  was observed. The energetic parameters,  $E_P$ ,  $E_D$ , and  $\Delta H_S$ , were obtained from the slope of the logarithmic plot of  $P$ ,  $D$ , and  $S$  on  $T^{-1}$  and are listed in Table 2, together with the prefactors  $\ln P_0$ ,  $\ln D_0$  and  $\ln S_0$ .

The PS control film had  $E_D$  of  $23.6 \text{ kJ mol}^{-1}$  in this temperature range, close to the value reported in the literature for glassy PS.<sup>44</sup> The PEO control film had higher  $E_D$  ( $45.3 \text{ kJ mol}^{-1}$ ) because the amorphous phase was in the rubbery state in this temperature range. All the PS/PEO 50/50 layered films had  $E_D$  of about  $55$  to  $60 \text{ kJ mol}^{-1}$ , without an obvious effect of layer thickness. The  $E_D$  of the layered film was close to that of the PEO control because the less permeable PEO layers dominated the permeability of the layered film. The fact that  $E_D$  was almost constant indicated that the diffusion jump length in the PEO layer was not affected by layer confinement.<sup>45</sup> The decrease in  $D$  with layer thickness was reflected only in the decrease in the preexponential factor  $D_0$ , Table 2.

In the temperature range studied, solubility of PS ( $S_{\text{PS}}$ ) was about 10 times higher than that of PEO ( $S_{\text{PEO}}$ ), because of the high crystallinity in PEO. Also PS and PEO differed in

the temperature dependence of  $S$  due to differences in the sorption mechanism in glassy and rubbery polymers.<sup>46</sup> The solubility of the PS/PEO layered films ( $S_{PS/PEO}$ ) should be a summation of the contributions from both layers

$$S_{PS/PEO} = \phi_{PS} S_{PS} + \phi_{PEO} S_{PEO} \quad (14)$$

where  $\phi_{PS}$  and  $\phi_{PEO}$  are the volume fractions of PS and PEO layers, respectively. The contribution of  $S_{PEO}$  was negligible, and the observed  $S$  was about  $0.5S_{PS}$  for the 50/50 films. In Figure 11c, the  $S$  vs  $T^{-1}$  data for the 50/50 films with

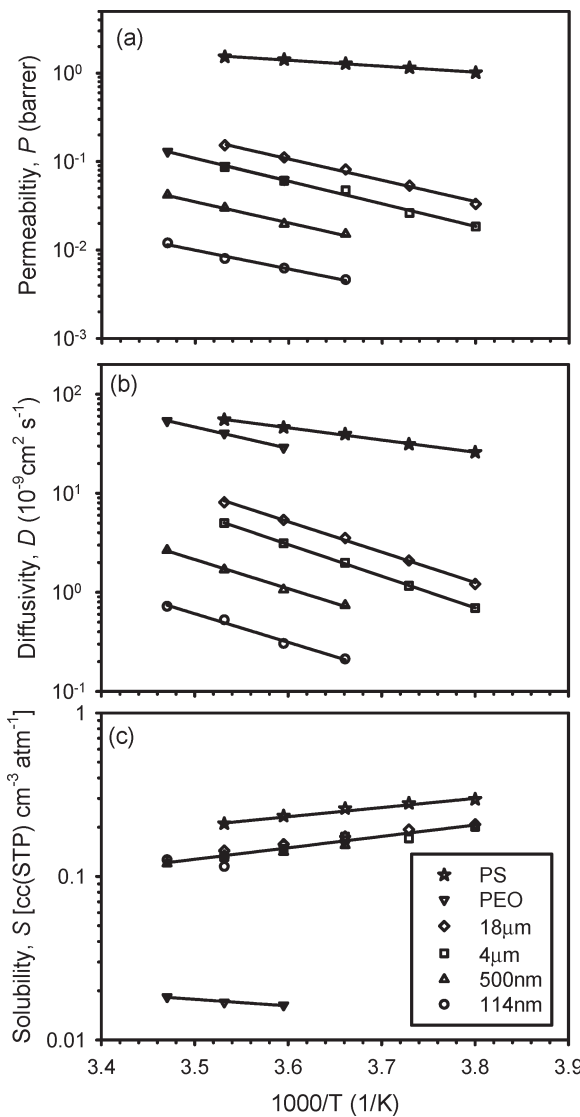


**Figure 11.** Temperature dependence of (a) oxygen permeability  $P$ , (b) oxygen diffusivity  $D$ , and (c) oxygen solubility  $S$  of PS and PEO controls and PS/PEO 50/50 layered films. The PEO layer thickness is as labeled.

different layer thicknesses fell on a single line with a common  $\Delta H_S$  of  $-13.4 \text{ kJ mol}^{-1}$ , close to the PS control value.

**Moisture Effect on Permeability.** The properties of PEO are significantly affected by the relative humidity (RH). The PEO control and the PEO layers dissolved at  $\text{RH} \geq 90\%$  at  $23^\circ\text{C}$ . Therefore 85% RH and  $23^\circ\text{C}$  were chosen as the conditions for measuring the moisture sorption and the oxygen permeability. Kinetic experiments showed that moisture sorption of the  $125 \mu\text{m}$  thick films increased during the first 3 days but reached a plateau after 4 days at 85% RH. The equilibrated moisture content after 7 days for films that differed in composition and in layer thickness (number of layers) is plotted in Figure 12 as a function of PEO weight content. The PS control film did not show any moisture sorption, whereas the PEO control film had a moisture sorption of 8.3 wt %. Moisture sorption of the PS/PEO layered films increased linearly with increasing PEO content. In addition, no layer thickness effect was observed among the 50/50 films with different layer thicknesses. It was concluded that the PEO layer absorbed the same amount of moisture as the PEO control.

The PS control film showed no change in  $P$  measured at 85% RH. The  $P$  of the PEO control film was not tested at 85% RH because the film became brittle and fractured in the diffusion cell. However an increase in  $P$  was observed in layered films. The  $P_{PEO,\text{eff}}$  at 85% RH was calculated from eq 6. Because the brittleness of the PEO films at 85% RH prevented direct measurement of  $P$ ,  $P_{PEO}$  at 85% RH was taken as  $P_{PEO,\text{eff}}$  at 85% RH for the thickest PEO layers ( $35 \mu\text{m}$ ). The resulting  $P_{PEO}$  was about double that at 0% RH. The results for  $P_{PEO,\text{eff}}$  at 85% RH are compared with  $P_{PEO,\text{eff}}$  at 0% RH in Figure 13. Although  $P_{PEO,\text{eff}}$  at 85% RH was generally 1.5 to 2 times higher than at 0% RH for all layer thicknesses, the dramatic drop in  $P_{PEO,\text{eff}}$  with layer thickness paralleled that at 0% RH. The WAXS patterns

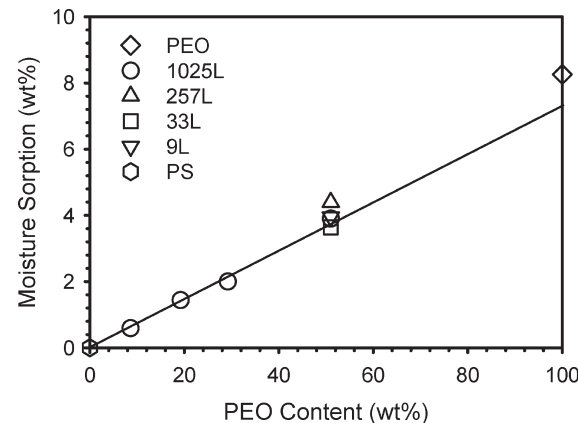


**Figure 12.** Equilibrated moisture sorption of PS/PEO layered films at 85% RH as a function of PEO content. The thickness of the films was about  $125 \mu\text{m}$ , and the key identifies the number of layers in the film. The standard deviation was within the size of the symbols.

**Table 2. Energetic Parameters of Oxygen Transport in PS/PEO 50/50 Layered Films and PS and PEO Controls**

sample	film thickness ( $\mu\text{m}$ )	nominal PEO layer thickness (nm)	$\ln P_0^a$	$E_P (\text{kJ mol}^{-1})$	$\ln D_0^a$	$E_D (\text{kJ mol}^{-1})$	$\ln S_0^a$	$\Delta H_S (\text{kJ mol}^{-1})$
PS control	5000		5.92	12.9	14.0	23.6	-6.1	-10.7
PEO control	5000		18.4	49.0	21.2	45.3	-0.78	7.7
9-layer	142	18000	17.7	46.1	27.1	58.8	-7.7	-13.4
33-layer	130	4000	18.4	48.9	27.6	61.2		
257-layer	127	500	15.8	45.6	24.5	56.3		
1025-layer	130	114	12.4	40.6	22.7	55.2		

<sup>a</sup>  $P_0$  in barrer,  $D_0$  in  $10^{-9} \text{ cm}^2 \text{s}^{-1}$ , and  $S_0$  in  $\text{cm}^3(\text{STP}) \text{ cm}^{-3} \text{ atm}^{-1}$

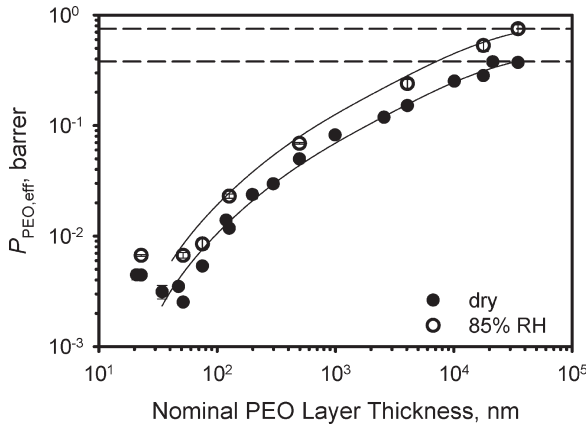


**Figure 13.**  $P_{PEO,eff}$  of PS/PEO layered films at 85% RH (○) and 0% RH (●) at 23 °C as a function of nominal PEO layer thickness. The solid lines are drawn as guides. The dashed lines indicate  $P_{PEO}$  at 0% RH (lower) and at 85% RH (upper).

confirmed that the in-plane lamellar orientation was not affected by the absorbed water (not shown here) and even under high RH the lamellae acted as impermeable platelets to dramatically reduce the oxygen permeability.

## Conclusions

Layer multiplying coextrusion uses forced assembly to create films with hundreds or thousands of alternating layers of two polymers. By decreasing the layer thickness from the microscale to the nanoscale, crystallization of a polymer in a confined, two-dimensional space can be studied. Forced assembly has many advantages over the methods conventionally used to study confined crystallization. The flexibility of the process allows confinement of almost any melt-processable polymer with a wide choice for the confining polymer. Here we studied the confined crystallization of PEO in microlayers and nanolayers confined by PS. As the PEO layer thickness decreased, the lamellar morphology changed from spherulites to flattened spherulites or discoids to in-plane lamellar stacks and finally to single-layered lamellae with large aspect ratio. The in-plane lamellar orientation in extruded nanolayers was much higher than that achieved in block copolymers. Indeed, the lamellae resembled the PEO single crystals that previously formed only in dilute solution. The growth of large in-plane crystals was thought to be facilitated by the low areal concentration of heterogeneous nuclei.

The large quantity of coextruded film obtained by the layer-multiplying coextrusion process enables the study of structure–property relationships of confined polymers. Oxygen permeability of PS/PEO layered films dramatically decreased as the layers became thinner. The confined, in-plane impermeable PEO lamellae with large aspect ratio imparted 2 orders of magnitude reduction in oxygen permeability. The effect of the confining polymer was demonstrated by comparing the results with PEO layers confined by EAA. The stronger confinement by the PS resulted in PEO layers with larger lamellae and lower permeability. A reduction in diffusivity due to the increased tortuosity of the diffusion pathway imparted the dramatic decrease in oxygen permeability. However, the temperature dependence of the diffusivity revealed that the activation energy was not affected by the PEO layer thickness, indicating that the diffusion jump length was not affected. Further evidence that confinement did not alter the solution-diffusion mechanism of oxygen transport was provided by the additive dependence of oxygen solubility. It is particularly noteworthy that even under high RH, the lamellae acted as impermeable platelets to dramatically reduce the oxygen permeability.

**Acknowledgment.** This research was supported by the NSF Center for Layered Polymeric Systems (Grant DMR-0423914).

## References and Notes

- Weinkauf, D. H.; Paul, D. R. In *Barrier Polymers and Structures*; Koros, W. J. Ed.; American Chemical Society: Washington, DC, 1990; Vol. 3, pp 60–91.
- Hiltner, A.; Liu, R. Y. F.; Hu, Y. S.; Baer, E. *J. Polym. Sci., Part B: Polym. Phys.* **2005**, *43*, 1047.
- Frank, C. W.; Rao, V.; Despotopoulou, M. M.; Pease, R. F. W.; Hinsberg, W. D.; Miller, R. D.; Rabolt, J. F. *Science* **1996**, *273*, 912.
- Reiter, G.; Botiz, I.; Gravelleau, L.; Grozev, N.; Albrecht, K.; Mourran, A.; Moeller, M. *Lect. Notes Phys.* **2007**, *714*, 179.
- Padden, F. J. Jr.; Keith, H. D. *J. Appl. Phys.* **1966**, *37*, 4013.
- (a) Douzinas, K. C.; Cohen, R. E. *Macromolecules* **1992**, *25*, 5030. (b) Hamley, I. W.; Fairclough, J. P. A.; Ryan, A. J.; Bates, F. S.; Towns-Andrews, E. *Polymer* **1996**, *37*, 4425. (c) Bartczak, Z.; Argon, A. S.; Cohen, R. E.; Kowalewski, T. *Polymer* **1999**, *40*, 2367. (d) Mellbring, O.; Oiseth, S. K.; Krozer, A.; Lausmaa, J.; Hjertberg, T. *Macromolecules* **2001**, *34*, 7496.
- (7) (a) Muratoglu, O. K.; Argon, A. S.; Cohen, R. E. *Polymer* **1995**, *36*, 2143. (b) Mukai, U.; Cohen, R. E.; Bellare, A.; Albalak, R. J. *J. Appl. Polym. Sci.* **1998**, *70*, 1985.
- (8) (a) Tsuji, M.; Novillo, F. A.; Fujita, M.; Murakami, S.; Kohjiya, S. *J. Mater. Res.* **1999**, *14*, 251–258. (b) Zhang, Y.; Mukoyama, S.; Hu, Y.; Yan, C.; Ozaki, Y.; Takahashi, I. *Macromolecules* **2007**, *40*, 4009.
- (9) Durell, M.; MacDonald, J. E.; Trolley, D.; Wehrum, A.; Jukes, P. C.; Jones, R. A. L.; Walker, C. J.; Brown, S. *Europhys. Lett.* **2002**, *58*, 844.
- (10) Zhu, L.; Cheng, S. Z. D.; Calhoun, B. H.; Ge, Q.; Quirk, R. P.; Thomas, E. L.; Hsiao, B. S.; Yeh, F. J.; Lotz, B. *J. Am. Chem. Soc.* **2000**, *122*, 5957.
- (11) Schonherr, H.; Frank, C. W. *Macromolecules* **2003**, *36*, 1188.
- (12) Sutton, S. J.; Izumi, K.; Miyaji, H.; Miyamoto, Y.; Miyashita, S. *J. Mater. Sci.* **1997**, *32*, 5621.
- (13) Bu, Z.; Welch, M. B.; Ho, R.-M.; Zhou, W.; Jangchud, I.; Eby, R. K.; Cheng, S. Z. D.; Hsieh, E. T.; Johnson, T. W.; Geerts, R. G. *Macromolecules* **1996**, *29*, 6575.
- (14) Abe, H.; Kikkawa, Y.; Iwata, T.; Aoki, H.; Akehata, T.; Doi, Y. *Polymer* **1999**, *41*, 867.
- (15) (a) Mareau, V. H.; Prud'homme, R. E. *Macromolecules* **2005**, *38*, 398–408. (b) Sun, Y. S.; Chung, T. M.; Li, Y. J.; Ho, R. M.; Ko, B. T.; Jeng, U. S.; Lotz, B. *Macromolecules* **2006**, *39*, 5782.
- (16) Ho, R. M.; Lin, F. H.; Tsai, C. C.; Lin, C. C.; Ko, B. T.; Hsiao, B. S.; Sics, I. *Macromolecules* **2004**, *37*, 5985.
- (17) Forrest, J. A.; Dalnoki-Veress, K.; Stevens, J. R.; Dutcher, J. R. *Phys. Rev. Lett.* **1996**, *77*, 2002.
- (18) Chen, Z. R.; Kornfield, J. A.; Smith, S. D.; Grothaus, J. T.; Satkowski, M. M. *Science* **1997**, *277*, 1248.
- (19) (a) Sluijters, R. *Mixing Apparatus* US Patent 3,051,453, Aug. 28, 1962. (b) Van der Hoeven, J. C.; Wimberger-Friedl, R.; Meijer, H. E. H. *Polym. Eng. Sci.* **2001**, *41*, 32.
- (20) (a) Liu, R. Y. F.; Jin, Y.; Hiltner, A.; Baer, E. *Macromol. Rapid Commun.* **2003**, *24*, 943. (b) Liu, R. Y. F.; Bernal-Lara, T. E.; Hiltner, A.; Baer, E. *Macromolecules* **2004**, *37*, 6972.
- (21) (a) Jin, Y.; Rogunova, M.; Hiltner, A.; Baer, E.; Nowacki, R.; Galeski, A.; Piorkowska, E. *J. Polym. Sci., Part B: Polym. Phys.* **2004**, *42*, 3380. (b) Bernal-Lara, T. E.; Liu, R. Y. F.; Hiltner, A.; Baer, E. *Polymer* **2005**, *46*, 3043. (c) Bernal-Lara, T. E.; Masirek, R.; Hiltner, A.; Baer, E.; Piorkowska, E.; Galeski, A. *J. Appl. Polym. Sci.* **2006**, *99*, 597.
- (22) Wang, H. P.; Keum, J. K.; Hiltner, A.; Baer, E.; Freeman, B.; Rozanski, A.; Galeski, A. *Science* **2009**, *323*, 757.
- (23) Huang, P.; Zhu, L.; Guo, Y.; Ge, Q.; Jing, A. J.; Chen, W. Y.; Quirk, R. P.; Cheng, S. Z. D.; Thomas, E. L.; Lotz, B.; Hsiao, B. S.; Avila-Orta, C. A.; Sics, I. *Macromolecules* **2004**, *37*, 3689.
- (24) (a) Mueller, C. D.; Nazarenko, S.; Ebeling, T.; Schuman, T. L.; Hiltner, A.; Baer, E. *Polym. Eng. Sci.* **1997**, *37*, 355. (b) Bernal-Lara, T. E.; Ranade, A.; Hiltner, A.; Baer, E. *Nano- and Microlayered Polymers: Structure and Properties*. In *Mechanical Properties of Polymers Based on Nanostructure*, 1st ed.; Micheler, G. H.; Balta-Callaja, F. Eds.; CRC Press: Boca Raton, FL 2005, p. 629.
- (25) Campbell, C.; Viras, K.; Richardson, M. J.; Masters, A. J.; Booth, C. *Makromol. Chem.* **1993**, *194*, 799.
- (26) Sekelik, D. J.; Stepanov, E. V.; Nazarenko, S.; Schiraldi, D.; Hiltner, A.; Baer, E. *J. Polym. Sci., Part B: Polym. Phys.* **1999**, *37*, 847.

- (27) Somlai, L. S.; Liu, R. Y. F.; Landoll, L. M.; Hiltner, A.; Baer, E. *J. Polym. Sci., Part B: Polym. Phys.* **2005**, *43*, 1230.
- (28) Balta Calleja, F. J.; Hay, I. L.; Keller, A. *Kolloid Z. Z. Polym.* **1966**, *209*, 128.
- (29) (a) Kautsky, J. A.; Walton, A. G.; Baer, E. *J. Appl. Phys.* **1967**, *38*, 1832. (b) Massa, M. V.; Carvalho, J. L.; Dalnoki-Veress, K. *Eur. Phys. J. E* **2003**, *12*, 111.
- (30) (a) Kautsky, J. A.; Walton, A. G.; Baer, E. *J. Polym. Sci., Polym. Lett.* **1967**, *5*, 185.
- (31) Tadokoro, H.; Chatani, Y.; Yoshihara, T.; Tahara, S.; Murahashi, S. *Makromol. Chem.* **1964**, *73*, 109.
- (32) Takahashi, Y.; Tadokoro, H. *Macromolecules* **1973**, *6*, 672.
- (33) Chen, J. H.; Cheng, S. Z. D.; Wu, S. S.; Lotz, B.; Wittmann, J. C. *J. Polym. Sci., Part B: Polym. Phys.* **1995**, *33*, 1851.
- (34) Hermans, P. H. *Contribution to the Physics of Cellulose Fibres*; Elsevier: Amsterdam, 1946; p 195.
- (35) White, J. L.; Choi, D. *Polyolefins: Processing, Structure Development, and Properties*; Hanser: Munich, Germany, 2005; Chapter 7.
- (36) 1 barrer =  $10^{10}[\text{cm}^3(\text{STP})\text{ cm}/(\text{cm}^2 \text{cmHg})]$ , where STP is standard temperature and pressure.
- (37) Liu, R. Y. F.; Hiltner, A.; Baer, E. *J. Polym. Sci., Part B: Polym. Phys.* **2004**, *42*, 493.
- (38) Gavara, R.; Hernandez, R. J. *J. Polym. Sci., Part B: Polym. Phys.* **1994**, *32*, 2375.
- (39) Jarus, D.; Hiltner, A.; Baer, E. *Polymer* **2002**, *43*, 2401.
- (40) Hu, Y. S.; Mehta, S.; Schiraldi, D. A.; Hiltner, A.; Baer, E. *J. Polym. Sci., Part B: Polym. Phys.* **2005**, *43*, 1365.
- (41) Cussler, E. L.; Hughes, S. E.; Ward, W. J. III; Aris, R. *J. Membr. Sci.* **1998**, *38*, 161.
- (42) Simon, F. T.; Rutherford, J. M. *J. Appl. Phys.* **1964**, *35*, 82–86.
- (43) Mandelkern, L.; Jain, N. L.; Kim, H. *J. Polym. Sci. Part A-2* **1968**, *6*, 165.
- (44) Guillet, J. E.; Andrews, M. *Macromolecules* **1992**, *25*, 2752.
- (45) Meares, P. *J. Am. Chem. Soc.* **1954**, *76*, 3415.
- (46) (a) Stern, S. A.; Trohalai, S. In *Barrier Polymers and Structures*; Koros, W. J., Ed.; American Chemical Society: Washington, DC, 1990; Vol. 2, pp 22–59. (b) Weiss, G. H.; Bendler, J. T.; Shlesinger, M. F. *Macromolecules* **1992**, *25*, 990. (c) Pauly, S. In *Polymer Handbook*, 3rd ed.; Brandrup, J., Immergut, E. H., Eds.; Wiley: New York, 1999; Chapter VI, pp 543–569.